Received: 9 December 2025 | Revised: 28 April 2026 | Accepted: 11 June 2026 | Published online: 7 July 2026

Journal of Optics and Photonics Research
2026, Vol. 00(00) 1–9
DOI: 10.47852/bonviewJOPR62028747
BON VIEW PUBLISHING

RESEARCH ARTICLE

Computational Investigation of Second Harmonic Generation in KTP Crystals Using COMSOL

Nabeel Ahmed[1, 2,*], **Muddasir Naeem**[2, 3] **and Tayyab Imran**[2, 4,*]

[1] *Department of Physics, COMSATS University Islamabad, Pakistan*

[2] *Group of Laser Development, Romania*

[3] *Department of Physics, Lahore University of Management Sciences, Pakistan*

[4] *National Institute for Research and Development in Microtechnologies, Romania*

Abstract: This study presents a COMSOL Multiphysics-based finite-element workflow for steady-state modeling of second harmonic generation (SHG) in potassium titanyl phosphate. The electromagnetic fields at the fundamental frequency ω and the second-harmonic frequency 2ω are solved in the frequency domain with explicit nonlinear polarization source terms, and the resulting photon flux trends are benchmarked against the standard depletion-included slowly varying envelope approximation under an idealized phase-matched condition ($\Delta k \sim 0$). Two pump wavelengths (1064 nm and 808 nm) and their corresponding SHG wavelengths (532 nm and 404 nm) are investigated, together with parametric variations of input intensity and an effective nonlinear coefficient used in the model. The results provide spatial field maps and photon flux evolution in a reproducible finite-element method setup; reported high conversion levels should be interpreted as upper-bound trends within the simplified, lossless benchmark assumptions rather than direct bulk experimental performance predictions. The present work can serve as a practical starting point for later extensions toward tensor-resolved, dispersion-aware, and fully three-dimensional SHG models.

Keywords: second harmonic generation, KTP crystal, COMSOL Multiphysics simulation, slowly varying envelope approximation

1. Introduction

Second harmonic generation (SHG) is a cornerstone process in the field of nonlinear optics, where two photons at the same fundamental frequency (ω) interact within a nonlinear medium to produce a single photon at twice the frequency (2ω) or half the wavelength. This frequency-doubling mechanism is essential in many advanced photonic applications, including high-efficiency laser systems, frequency-agile light sources, biomedical imaging techniques, fiber-optic communication, and quantum information processing [1–5]. A well-known example is the conversion of infrared laser light into the visible spectrum, which allows for expanded wavelength coverage in compact laser systems [6, 7].

However, realizing efficient SHG in practical systems presents several challenges. High optical intensities are required to stimulate nonlinear polarization, and phase-matching conditions must be strictly maintained to ensure constructive interference of the generated second harmonic wave [8, 9]. Moreover, the nonlinear crystal must exhibit favorable properties such as large second-order nonlinear coefficients [10], low absorption across the operating wavelengths [11], and high resistance to laser-induced damage [12, 13]. Potassium titanyl phosphate (KTP) crystals fulfill many of these criteria, making them highly attractive for SHG, especially in high-power or pulsed laser systems. Their broad transparency range, high thermal conductivity, and excellent phase-matching capabilities support their widespread adoption of commercial and research-grade optical frequency converters [14, 15].

Despite these material advantages, optimizing SHG systems using KTP requires a detailed understanding of the internal electromagnetic interactions that occur within the crystal. Traditional approaches to modeling SHG have often been limited to analytical formulations, such as those based on the slowly varying envelope approximation (SVEA) [16, 17] or simplified geometrical ray-tracing techniques. While these provide foundational insights, they do not capture the full spatial and spectral complexity of SHG [18], particularly when dealing with high-intensity fields, non-uniform beam profiles, and realistic boundary conditions [19, 20].

The present study employs COMSOL Multiphysics, a finite-element analysis platform, to simulate the SHG process in

---

***Corresponding author:** Nabeel Ahmed, Department of Physics, COMSATS University Islamabad, Pakistan and Group of Laser Development, Romania. Email: nabeelehmedrll@gmail.com and fa19-rph-023@isbstudent.comsats.edu.pk and Tayyab Imran, Group of Laser Development, Romania and National Institute for Research and Development in Microtechnologies, Romania. Email: tayyab.imran@imt.ro

KTP crystals within an idealized benchmark framework. Using the Wave Optics Module in frequency-domain mode, we solve Maxwell's equations for the fundamental and second harmonic fields under nonlinear coupling conditions. In the present implementation, nonlinear polarization source terms are introduced in a spatially resolved 2D frequency-domain model using an effective scalar treatment for the modeled polarization component [21–23]. By simulating two-dimensional field propagation in the KTP crystal, we examine benchmark trends showing how input intensity, nonlinear coupling strength, and fundamental wavelength influence the field evolution and photon flux behavior within the stated assumptions [24, 25].

Unlike studies based only on analytical treatment, the present work combines numerical simulation with benchmarking against analytical results derived from SVEA. This comparison is used here as a consistency check for the implemented benchmark formulation under matched assumptions, rather than as proof of full physical realism or device-level validation. The field plots and photon flux distributions generated in COMSOL are therefore interpreted as spatially resolved benchmark results that follow the expected qualitative SHG trends, including depletion of the fundamental wave and growth of the harmonic field [16–19].

Furthermore, COMSOL provides a practical environment for exploring parameter variations that would be more time-consuming to test experimentally. Within the present benchmark assumptions, the simulations show that the SHG trend strengthens with increasing input intensity and with the effective nonlinear coupling parameter and that the 808 nm case exhibits faster photon flux evolution over the same interaction length than the 1064 nm case. These observations should not be generalized directly to device-level performance without including full dispersion, tensor anisotropy, walk-off, absorption, and damage-threshold constraints. This study therefore demonstrates the usefulness of COMSOL-based modeling as a transparent benchmark workflow for visualizing nonlinear optical trends and for supporting future extensions toward more realistic nonlinear-device simulations.

In this work, the primary contribution is a reproducible COMSOL implementation template for coupled ω and 2ω full-wave fields using explicit nonlinear polarization source terms, together with spatially resolved field visualizations and a benchmark comparison to the well-known phase-matched SVEA solution. The study is presented as an idealized benchmark case (effective scalar d_{eff}, $\Delta k \approx 0$, no linear loss, and 2D geometry) to enable direct comparison with analytical predictions; extensions to full tensor-rotated KTP anisotropy, birefringent phase matching, and 3D beam propagation are discussed as future work. Even within this simplified scope, the model remains useful because it provides a clear teaching and benchmarking framework for setting up coupled ω and 2ω simulations in COMSOL. It also helps visualize how the fundamental and harmonic fields evolve spatially within the simulated geometry, which is harder to see from compact 1D analytical expressions alone. In this sense, the present work can serve as a practical starting point for later extensions toward tensor-resolved, dispersion-aware, and fully three-dimensional SHG models.

2. COMSOL Multiphysics Simulation of SHG

2.1. Methodology

COMSOL Multiphysics was employed with the Wave Optics Module operating in the frequency domain to model SHG in KTP crystals. The goal is to simulate the full nonlinear electromagnetic interaction between the fundamental and second harmonic fields with spatial and spectral accuracy. The modeling sequence, outlined conceptually in Figure 1, was implemented in a stepwise workflow: defining crystal geometry, assigning material properties, applying electromagnetic wave equations, coupling via nonlinear polarization terms, generating the mesh, solving Maxwell's equations, and finally post-processing electric-field results.

Figure 1

Simulation workflow for SHG modeling in KTP using COMSOL

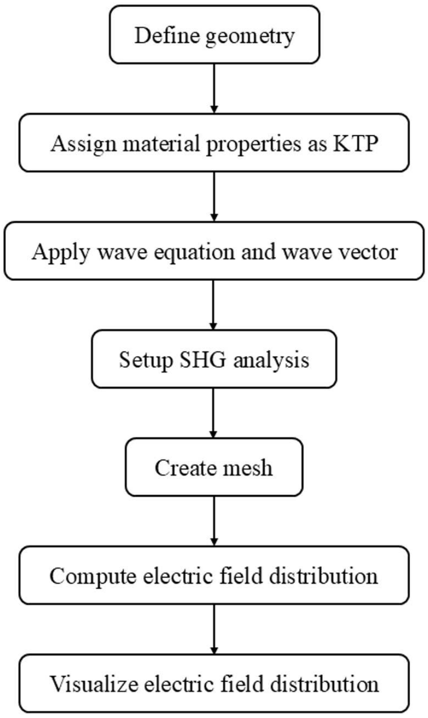

To simulate SHG, nonlinear polarization source terms were added to the governing Maxwell's equations in an effective scalar form for the modeled polarization component (2D, E_y). The nonlinear polarizations are written as $P_y(2\omega) = 2\varepsilon_0 \, d_{eff} \, [E_y(\omega)]^2$ for SHG generation and $P_y(\omega) = 2\varepsilon_0 d_{eff} E_y(2\omega) E_y^*(\omega)$ for depletion/back-coupling. In COMSOL, these polarizations are implemented as equivalent current sources $J_y(\Omega) = -i\Omega P_y(\Omega)$ in the respective frequency-domain interfaces ($\Omega = \omega$ or 2ω). This coupled-source steady-state formulation is used here as an idealized benchmark for comparison with the phase-matched SVEA model.

To emulate an open domain and reduce reflections at the outer boundaries, we used COMSOL's Scattering Boundary Condition, which functions as an absorbing (open) boundary condition (ABC) for outgoing waves (alternatively, a perfectly matched layer (PML) can be used for stronger absorption). The computational domain was meshed with a physics-controlled mapped mesh to ensure adequate spatial resolution across the nonlinear interaction region, and the overall workflow (geometry, materials, interfaces, coupling, solvers, and post-processing) was verified for consistency using SVEA trends as a baseline [26].

Boundary conditions (open/absorbing): To approximate an unbounded domain, the outer boundaries were assigned an outgoing-wave absorbing condition. In electromagnetic form, this can be written as a first-order Sommerfeld-type condition on the tangential field: $n \times (\nabla \times \mathrm{E}(\Omega)) = i\,\mathrm{k}(\Omega)\, n \times (n \times \mathrm{E}(\Omega))$, where n is the outward unit normal and $k(\Omega) = n_r(\Omega)\cdot\Omega/c$ is the wavenumber in the surrounding medium. This condition is applied consistently for both $\Omega = \omega$ (fundamental) and $\Omega = 2\omega$ (second harmonic). In COMSOL, this is implemented via the built-in Scattering Boundary Condition, which functions as an absorbing/open boundary (ABC). For stronger absorption (especially for oblique components), a PML can be used as an alternative.

Sequential frequency-domain strategy: The present formulation is numerically useful because it allows the nonlinear source terms at ω and 2ω to be implemented in a transparent and reproducible way within the COMSOL environment. At the same time, we stress that this approach is used here as a steady-state benchmark strategy and not as a replacement for a fully self-consistent broadband time-domain treatment. Accordingly, the reported finite element method (FEM)–SVEA agreement is interpreted as a consistency check of the implemented coupling framework under matched assumptions rather than as a complete proof of global energy exchange accuracy for realistic pulsed SHG.

Numerical accuracy: To assess numerical reliability, we performed mesh-refinement checks by increasing the mesh density (elements per wavelength) in the nonlinear interaction region and verifying that the field-map features and photon flux trends remained stable. Residual numerical error is primarily associated with discretization and the sequential coupled-source frequency-domain strategy; the reported results are therefore interpreted as benchmark trends under the stated assumptions discussed in Table 1.

Phase matching and wave-vector mismatch: In this benchmark study, we consider an idealized phase-matched condition with $\Delta k = k_{2\omega} - 2k_{\omega} \approx 0$, as mentioned in Table 1, so that the FEM results can be directly compared with the standard closed-form SVEA expressions used in Equations (1) and (2). A full birefringent KTP treatment would require (i) dispersion relations (Sellmeier equations) to compute $n(\omega)$ and $n(2\omega)$ and (ii) rotation of the $\chi^{(2)}$ tensor to a chosen crystal cut and polarization configuration (Type-I/Type-II) to determine the relevant $\mathrm{d_{ij}}$ and $\mathrm{d_{eff}}$; these extensions are outside the scope of the present benchmark and are noted for future work.

A range of simulation parameters was explored, as summarized in Table 2. The two fundamental wavelengths used, 1064 nm and 808 nm, correspond to commonly used laser sources, and their associated SHG wavelengths were 532 nm and 404 nm. Input intensities of 30 MW/m² and 50 MW/m² are used as steady-state (CW-equivalent) intensity levels to set the field amplitudes in the frequency-domain model; for ultrashort pulses, these values would correspond to an effective peak intensity, and a time-domain treatment would be required to capture temporal effects such as group-velocity mismatch. Two values of an effective nonlinear coefficient $\mathrm{d_{eff}}$ were used to evaluate the sensitivity of the SHG trends to nonlinear coupling strength. The chosen $\mathrm{d_{eff}}$ values should be regarded as effective model parameters for the implemented source term (not a direct mapping to a specific KTP tensor element without an explicit orientation/polarization configuration), as summarized in Table 3.

This full-wave, frequency-domain simulation approach offers several advantages over simplified models within the scope of the present benchmark study: it provides spatially resolved field evolution, beam propagation behavior in the simulated 2D slice, depletion trends, and interference features [27]. In particular, it allows direct visual observation of electric-field evolution and energy transfer between the fundamental and SHG components under the stated assumptions. As a result, the present modeling

Table 1
Comparison between the standard SVEA description and the present FEM benchmark workflow

Feature	SVEA	Present FEM benchmark
Model type	1D analytical coupled-wave description	2D frequency-domain numerical workflow with explicit nonlinear source terms
Main strength	Fast analytical benchmark for photon flux evolution	Provides spatial field maps and a reproducible COMSOL implementation pathway
Boundary treatment	Usually implicit or simplified	Includes explicit computational geometry and open-boundary treatment
What it does not capture	Detailed spatial field distributions in the simulated cross-section	Full tensor anisotropy, rigorous Δk calculation for a specific cut, full 3D propagation, and time-domain pulse effects are not yet included

Table 2
Parameters used in COMSOL modeling

Parameter	Value(s)	Description
λ_1	1064 nm, 808 nm	Fundamental wavelength
$\mathrm{f_1}$	c/λ_1	Frequency of the fundamental wave
$\mathrm{f_2}$	$2\mathrm{f_1}$	Frequency of the SHG wave
λ_2	532 nm, 404 nm	SHG wavelength
d	1.0×10^{-18}, 1.4×10^{-18}	Effective nonlinear coefficient $\mathrm{d_{eff}}$ used in source term (SI scaling parameter; m/V)
$\mathrm{I_1}$	30 MW/m^2, 50 MW/m^2	Input intensity (steady-state/CW-equivalent level)
L	1.7776×10^{-5} m	Length of nonlinear region

Table 3
Summary of key model assumptions used in the present benchmark formulation

Assumption	Why used here	Limitation/consequence
$\Delta k \approx 0$ (idealized phase matching)	To enable direct comparison with standard phase-matched SVEA expressions	Not a quantitative phase-matching calculation for a specific KTP cut or polarization state
Effective scalar d_eff	To implement nonlinear source coupling in a simple 2D benchmark form	Does not represent full tensor-rotated $\chi(2)$ anisotropy of KTP
2D geometry	To keep the model computationally manageable and visually clear	Does not capture full 3D beam structure, second transverse diffraction, or walk-off
Lossless medium	To isolate benchmark SHG trends without additional dissipative effects	May overestimate conversion trends relative to practical devices
CW-equivalent input intensity	To define steady-state field amplitudes in the frequency-domain formulation	Does not include ultrashort-pulse effects such as temporal walk-off or spectral broadening
Sequential coupled-source frequency-domain solve	To provide a transparent and reproducible numerical workflow in COMSOL	Not equivalent to a fully coupled broadband time-domain energy-conserving treatment

strategy is best viewed as a reproducible benchmark workflow that may serve as a starting point for later, more realistic design-oriented models rather than as a complete predictive tool for crystal selection or device optimization.

2.2. Analysis and discussion

Model scope and limitations: The simulations are performed in 2D as a planar slice to provide clear visualization and manageable computational cost. As a consequence, diffraction in the second transverse dimension, full 3D mode structure, and birefringent walk-off are not captured. The present results are therefore interpreted as benchmark trends under idealized assumptions (effective scalar d_{eff}, $\Delta k \approx 0$, lossless medium) rather than direct predictions for a specific 3D bulk KTP device.

Figure 2(a) shows the corresponding distribution of the fundamental wave at 1064 nm. The field intensity is high near the input surface of the crystal and gradually decreases along the propagation direction. This decay in field strength directly indicates energy being transferred from the fundamental wave to the second harmonic wave through the nonlinear process. The pattern near the source displays stronger oscillations and higher electric-field values, which diminish as the wave progresses, reflecting the conversion of optical energy into the SHG field. This dynamic illustrates the fundamental principle of SHG, where the pump wave loses intensity in favor of the newly generated frequency-doubled component.

In contrast, in Figure 2(b), which corresponds to the SHG field at 532 nm, the electric field exhibits a well-defined periodic pattern extending uniformly across the width of the crystal. The alternating red and blue fringes denote constructive and destructive interference regions, signifying a coherent and efficient generation of the second harmonic wave. The spatially regular pattern indicates that the benchmark assumes an idealized phase-matched condition ($\Delta k \approx 0$), leading to effective frequency doubling within the crystal. The intensity remains consistent throughout the propagation length, confirming a stable nonlinear interaction. Figure 2(c), representing the fundamental wave at 808 nm, also displays a distinct field intensity pattern, with high values concentrated near the input and gradually decreasing as the wave propagates through the medium. This again confirms the progressive transfer of energy to the SHG field. Due to the higher frequency, the oscillations are more tightly spaced compared to, reflecting the shorter wavelength of the wave. The fine structure in the field profile illustrates the impact of dispersion and wave vector mismatch on the spatial properties of the interaction. Figure 2(d) displays the second harmonic field at 404 nm, showing a highly periodic and coherent field pattern throughout the crystal. The regularity and uniformity of the pattern suggest efficient generation and propagation of the second harmonic wave within the assumed phase-matched benchmark ($\Delta k \approx 0$). The increased frequency results in finer spatial oscillations, which are visible in the denser fringe pattern compared to its lower-frequency counterpart. This clearly illustrates the wavelength dependence of SHG efficiency and propagation behavior.

Figure 2 illustrates the spatial evolution of the fundamental and second harmonic fields along the propagation direction in the benchmark configuration. The maps qualitatively show energy transfer from the fundamental wave to the generated second harmonic through the nonlinear coupling term, and they provide spatial context that is not available from 1D coupled-wave expressions alone. In this work, these field maps are used primarily for visualization and consistency checking under the assumed phase-matched condition ($\Delta k \approx 0$).

The simulation results are benchmarked using the SVEA [19] to derive analytical expressions for photon flux density. These spatial maps are useful because they show where depletion of the fundamental field and buildup of the harmonic field occur within the simulated geometry. This visual information complements the SVEA curves by linking the photon flux trends to the field distribution inside the computational domain. Photon flux densities were calculated to quantify energy conversion using the following relations in Equations (1) and (2):

For a fundamental wave,

$$\Phi_1(x) = \Phi_1(0)\,\mathrm{sech}^2(\gamma x/2) \tag{1}$$

Figure 2
Normalized electric-field intensity maps (proportional to $|E|^2$, in arbitrary units) inside the KTP region for (a) fundamental wave at 1064 nm, (b) SHG wave at 532 nm, (c) fundamental wave at 808 nm, and (d) SHG wave at 404 nm

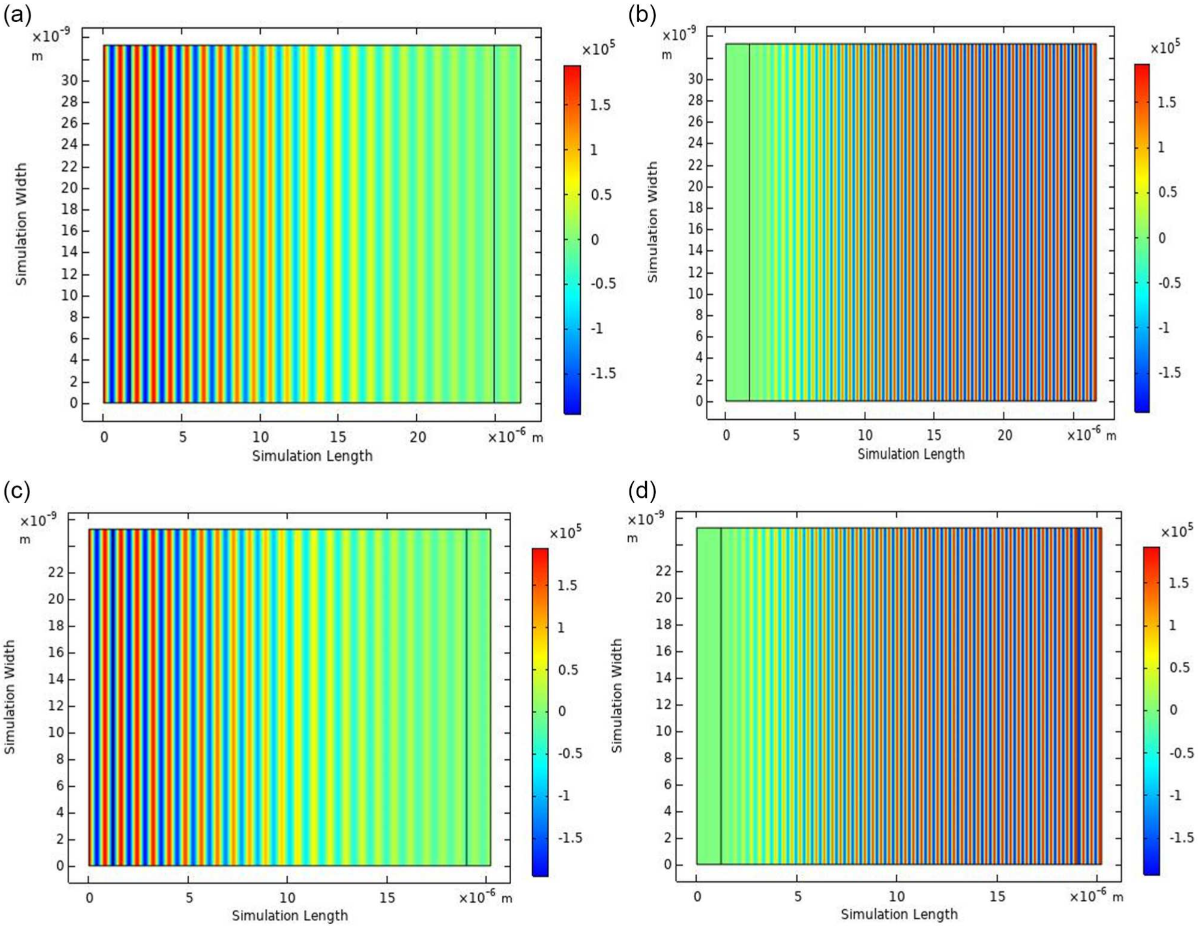

For the second harmonic wave,

$$\Phi_2(x) = 1/2 \times \Phi_1(0) \tanh^2(\gamma x/2) \qquad (2)$$

where γ is the gain coefficient given by $\gamma = 8\,(d_{eff})^2\,(Z_0)^3\,\omega^3\,I_1(0)$ [19] and Z_0 denotes the wave impedance of the medium (for a non-magnetic dielectric, $Z_0 \approx Z_{vac}/n$).

Figure 3 compares the crystal's 1064 nm and 808 nm electric-field intensities. The blue curve represents the fundamental field in each case, while the green curve corresponds to the SHG field. At the beginning of the interaction (near $x = 0$), the fundamental wave dominates with high-amplitude oscillations, while the SHG wave is initially weak. As the waves propagate, the amplitude of the fundamental field gradually decreases while the SHG field increases, indicating an efficient nonlinear frequency conversion process. Notably, the SHG field reaches a saturation level, where its growth stabilizes, indicating the limit of energy that can be transferred under phase-matched conditions.

Figure 4 illustrates the evolution of the photon flux density of the fundamental and second harmonic waves along the x-direction within the crystal for two different input intensities: 30 MW/m² and 50 MW/m², respectively. The red lines show the photon flux density of the fundamental wave, and the cyan lines show the photon flux density of the second harmonic wave. Comparing the two figures reveals that at 50 MW/m² input intensity, the SHG buildup begins earlier and reaches a higher amplitude compared to the 30 MW/m² case, thereby confirming that stronger input intensities lead to earlier and more efficient SHG conversion due to higher nonlinear interaction strength.

Figure 5 further extends this investigation by analyzing the photon flux density of both waves by changing the value of the nonlinear coefficient, which effectively changes the nonlinear response of the crystal. These graphs include both simulated data points and theoretical predictions based on the SVEA [15, 16], allowing for a direct comparison of numerical accuracy. The red and cyan lines represent SVEA results, while the blue and green markers denote the fundamental and SHG wave simulation results. Figures 5(a) and (c) correspond to a lower nonlinear coefficient (denoted as d), and Figures 5(b) and (d) use a higher value of nonlinear coefficient (d), but the length of the nonlinear region remained the same, 1.7776 x 10^{-5} m. In both cases, the plots exhibit a characteristic exchange in photon flux: the fundamental photon flux decreases exponentially, while the SHG photon flux rises until it reaches saturation. Importantly, the figures demonstrate that a larger nonlinear coefficient enhances the crystal polarization response, significantly boosting the SHG photon flux density and leading to more effective energy transfer. This confirms theoretical expectations that SHG efficiency is directly proportional to the square of the nonlinear coefficient,

Figure 3
Electric-field intensities comparison for (a) fundamental (1064 nm) and second harmonic wave (532 nm) and (b) fundamental (808 nm) and second harmonic wave (404 nm)

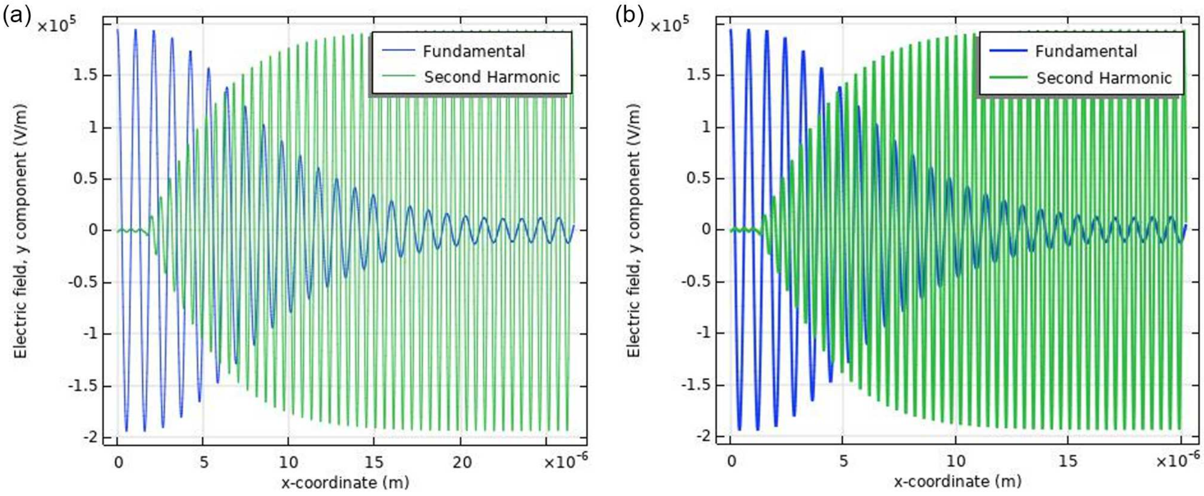

Figure 4
Photon flux density of 808 nm at (a) 30 MW/m^2 and (b) 50 MW/m^2. Photon flux density of 1064 nm at (c) 30 MW/m^2 and (d) 50 MW/m^2

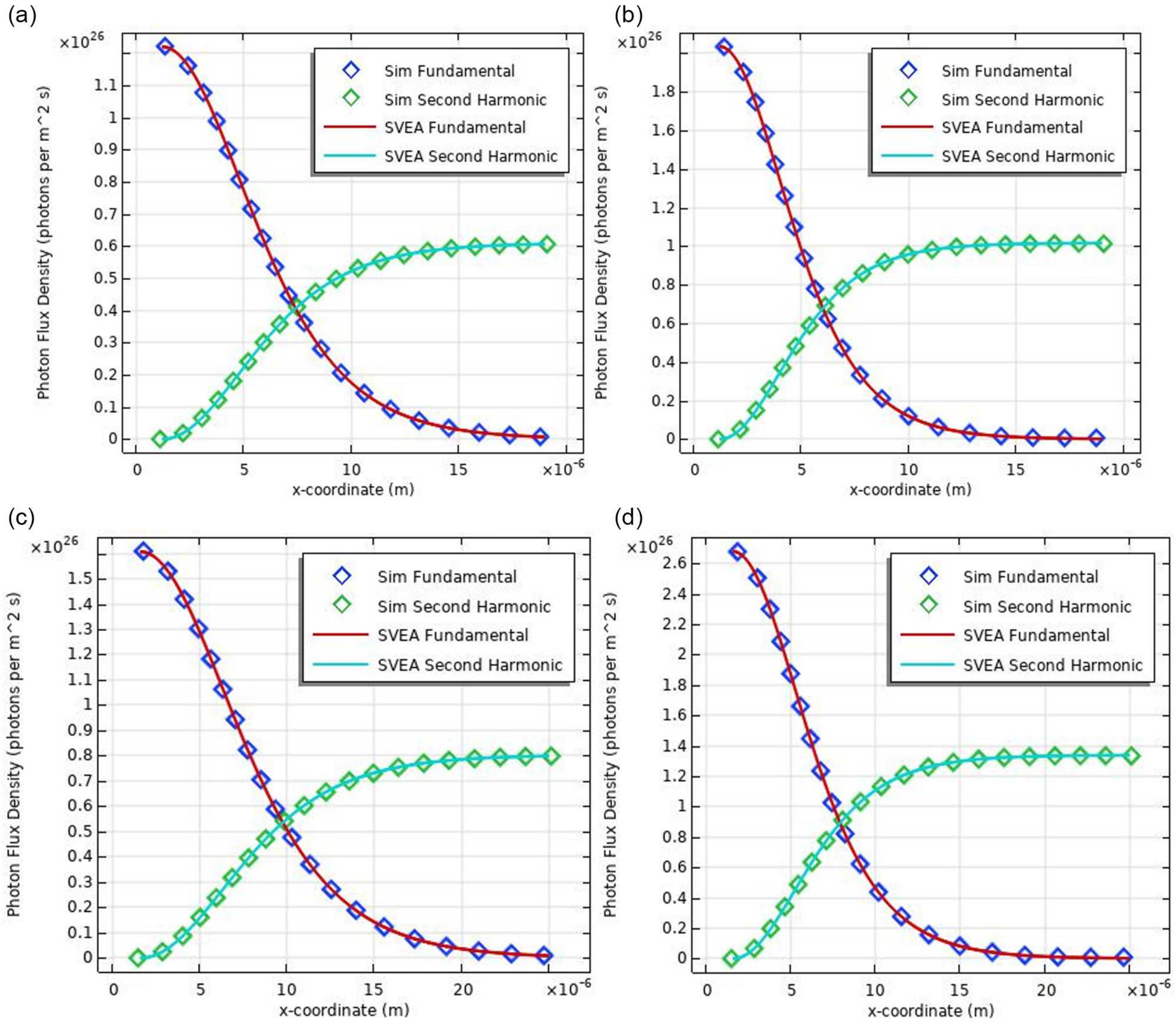

Figure 5
Photon flux density of 808 nm at (a) $d = 1 \times 10^{-18}$ C/V^2 and (b) $d = 1.4 \times 10^{-18}$ C/V^2. Photon flux density of 1064 nm at (c) $d = 1 \times 10^{-18}$ C/V^2 and (d) $d = 1.4 \times 10^{-18}$ C/V^2

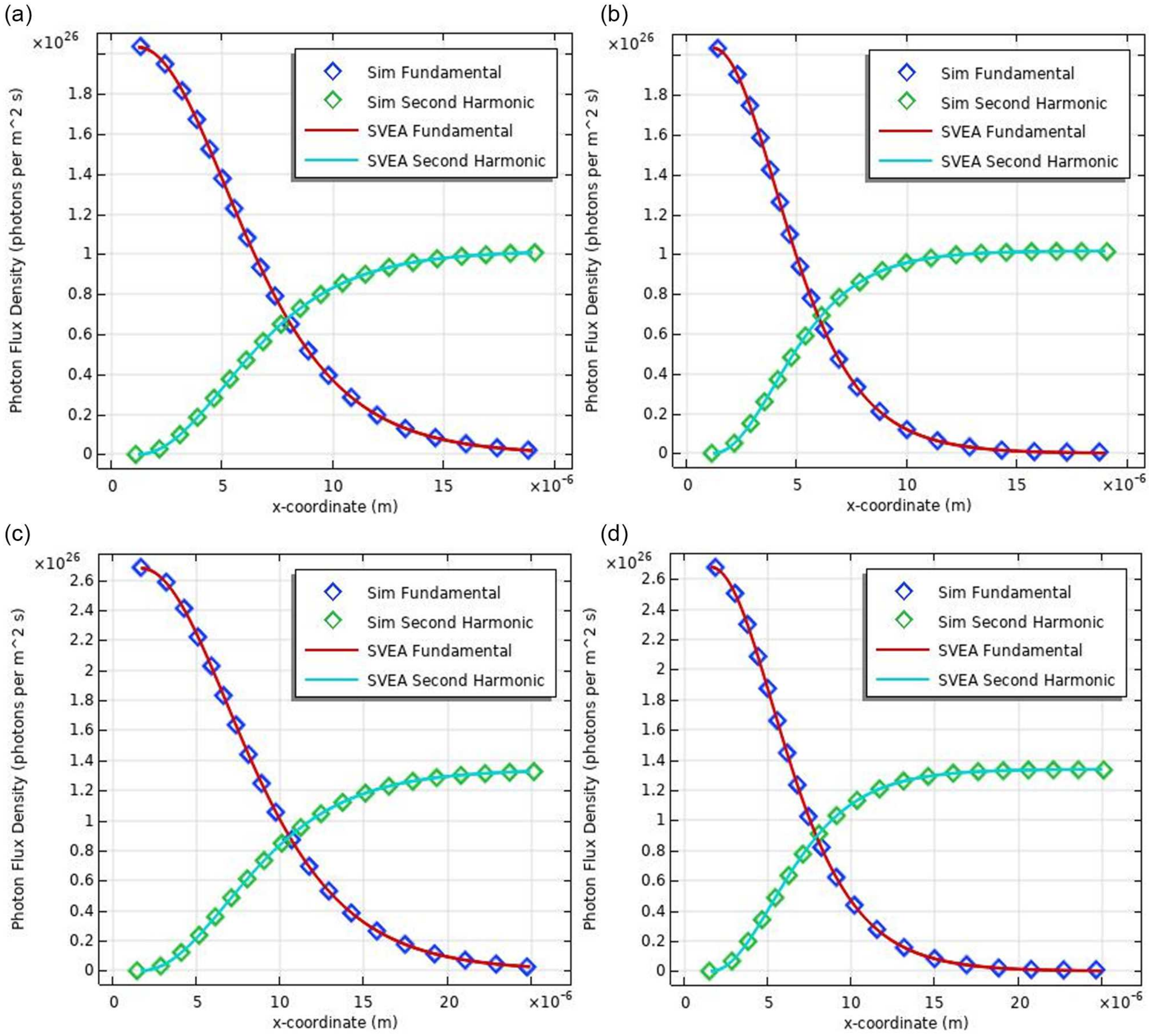

emphasizing the importance of material selection and optimization for frequency conversion applications.

These results are discussed here in the context of benchmark SHG trends in KTP, a material known for strong nonlinear optical performance and favorable phase-matching behavior. Within the present model, the variation of input intensity and effective nonlinear coupling parameter helps illustrate how energy is redistributed between the fundamental and harmonic fields under steady-state (CW-equivalent) excitation. These observations are intended to provide qualitative and semi-quantitative guidance within the benchmark framework, while more realistic optimization of SHG output would require a fuller treatment of crystal orientation, anisotropy, dispersion, absorption, and 3D propagation.

Photon conversion efficiency was found to approach 50% only within the idealized benchmark conditions used in this study. Here, the photon conversion efficiency is defined as $\eta_{\text{photon}} = \Phi_2/\Phi_1(0)$. Under the idealized lossless, phase-matched SHG benchmark ($\Delta k \approx 0$), depletion-included SVEA predicts an asymptotic upper bound $\Phi_2 \to 0.5\ \Phi_1(0)$. Therefore, values approaching 50% in this manuscript should be interpreted as an upper-bound trend of the benchmark model rather than a direct bulk experimental efficiency for an 18 μm KTP crystal.

Figure 6 presents a comparative analysis of SHG efficiency between two fundamental wavelengths, specifically 808 nm and 1064 nm, using photon flux density as the key metric. These plots are crucial in understanding the wavelength dependence of nonlinear optical processes in KTP crystals. In both figures, the blue diamonds represent the simulated photon flux density of the fundamental wave, while the green diamonds show the corresponding SHG wave. The red and cyan lines indicate theoretical photon flux densities for the fundamental and SHG waves. As in earlier figures, the general trend reflects the conservation of energy: the fundamental wave gradually loses photons as the wave propagates, while the SHG wave gains photons, reaching a saturation level beyond which further conversion is minimal.

Despite the visual similarity in the shape and pattern, Figure 6 focuses on how the input wavelength influences the SHG trends within the benchmark model. Specifically, Figure 6(a) corresponds to the fundamental wavelength of 808 nm, while

Figure 6
Photon flux density profiles for both fundamental and second harmonic waves at (a) 808 nm and (b) 1064 nm, showing good agreement between simulation (Sim) and SVEA results

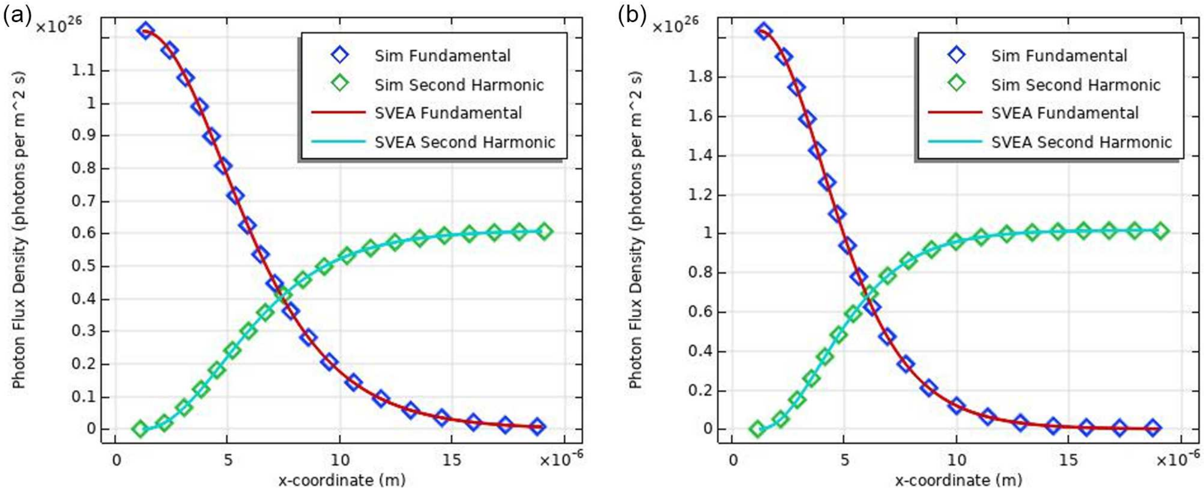

Figure 6(b) represents the 1064 nm case. Within the steady-state, phase-matched ($\Delta k \approx 0$) and lossless assumptions used here, the 808 nm case shows faster depletion of the fundamental photon flux and a more rapid increase of the SHG photon flux over the same interaction length, consistent with the corresponding SVEA trends. These comparisons are intended as a consistency check between the FEM workflow and the analytical benchmark under matched assumptions, rather than a direct optimization statement for a particular 3D bulk device where additional effects (e.g., walk-off, diffraction, absorption, damage threshold) would need to be included.

3. Conclusion

This study presents a COMSOL-based finite-element workflow for steady-state modeling of SHG in KTP using coupled ω and 2ω frequency-domain electromagnetic solves with explicit nonlinear polarization source terms. The methodology (Figure 1) is intended as a step-by-step template that enables reproducible setup of geometry, materials, wave interfaces, nonlinear coupling, and post-processing. The simulations illustrate how SHG trends depend on input wavelength, intensity level, and the effective nonlinear coupling parameter used in the model, and they provide spatial field maps together with photon flux evolution along the propagation direction. Benchmark comparisons with depletion-included SVEA expressions under the same idealized phase-matched assumption ($\Delta k \approx 0$) show consistent trends, serving as a numerical cross-check of the implemented coupling strategy. Because the present study is a 2D, lossless benchmark with an effective scalar d_{eff} and without birefringent walk-off or full tensor-rotated anisotropy, the reported high conversion levels should be interpreted as upper-bound trends within the simplified model. Future extensions will incorporate explicit KTP tensor orientation, dispersion-based Δk evaluation, and 3D beam propagation to support direct device-level predictions.

A natural next step of this work is to extend the present benchmark formulation toward a more realistic device-level model. In particular, future studies should incorporate Sellmeier-based refractive indices, explicit tensor rotation of the $\chi(2)$ coefficients, specific Type-I or Type-II phase-matching configurations, three-dimensional beam propagation, pulsed time-domain effects, and direct comparison with experimental measurements. Such extensions would allow the present workflow to evolve from a benchmark visualization framework into a more predictive modeling tool for practical SHG design in KTP.

Ethical Statement

This study does not contain any studies with human or animal subjects performed by any of the authors.

Conflicts of Interest

The authors declare that they have no conflicts of interest to this work.

Data Availability Statement

The data that support the findings of this study are available within the article.

Author Contribution Statement

Nabeel Ahmed: Conceptualization, Methodology, Software, Formal analysis, Resources, Data curation, Writing – original draft, Writing – review & editing, Visualization. **Muddasir Naeem:** Validation, Formal analysis, Resources, Data curation, Writing – original draft, Writing – review & editing, Visualization, Supervision. **Tayyab Imran:** Conceptualization, Methodology, Validation, Investigation, Resources, Data curation, Writing – original draft, Writing – review & editing, Supervision, Project administration.

References

[1] Solgi, S., Tafreshi, M. J., & Ghamsari, M. S. (2019). Nonlinear optical crystals for second harmonic generation. *Crystallography Reports*, *64*(7), 1138–1149. https://doi.org/10.1134/S1063774519070204

[2] Chen, J., Hu, C.-L., Kong, F., & Mao, J.-G. (2021). High-performance second-harmonic-generation (SHG) materials: New developments and new strategies. *Accounts of Chemical*

Research, *54*(12), 2775–2783. https://doi.org/10.1021/acs.accounts.1c00188

[3] Huang, W., Xiao, Y., Xia, F., Chen, X., & Zhai, T. (2024). Second harmonic generation control in 2D layered materials: Status and outlook. *Advanced Functional Materials*, *34*(16), 2310726. https://doi.org/10.1002/adfm.202310726

[4] Aghigh, A., Bancelin, S., Rivard, M., Pinsard, M., Ibrahim, H., & Légaré, F. (2023). Second harmonic generation microscopy: A powerful tool for bio-imaging. *Biophysical Reviews*, *15*(1), 43–70. https://doi.org/10.1007/s12551-022-01041-6

[5] James, D. S., & Campagnola, P. J. (2021). Recent advancements in optical harmonic generation microscopy: Applications and perspectives. *BME Frontiers, 2021*, *3973857*. https://doi.org/10.34133/2021/3973857

[6] Hong, L., Liu, L., Liu, Y., Qian, J., Feng, R., Li, W., . . . , & Li, Z.-Y. (2023). Intense ultraviolet–visible–infrared full-spectrum laser. *Light: Science & Applications*, *12*(1), 199. https://doi.org/10.1038/s41377-023-01256-6

[7] Imran, T., Naeem, M., & Hussain, M. (2024). An experimental study of intensity-phase characterization of femtosecond laser pulses propagated through a polymethyl methacrylate. *Microwave and Optical Technology Letters*, *66*(6), e34217. https://doi.org/10.1002/mop.34217

[8] Dorrer, C., Begishev, I. A., Bahk, S.-W., & Bromage, J. (2022). High-resolution mapping of phase-matching conditions in second-order nonlinear crystals. *Optical Materials Express*, *12*(9), 3679–3695. https://doi.org/10.1364/OME.468127

[9] Zhang, W., Yu, H., Wu, H., & Halasyamani, P. S. (2017). Phase-matching in nonlinear optical compounds: A materials perspective. *Chemistry of Materials*, *29*(7), 2655–2668. https://doi.org/10.1021/acs.chemmater.7b00243

[10] Xie, Z., Zhao, T., Yu, X., & Wang, J. (2024). Nonlinear optical properties of 2D materials and their applications. *Small*, *20*(34), 2311621. https://doi.org/10.1002/smll.202311621

[11] Holland, K. M., Alejandro, A., Ludlow, D. J. H., Petersen, P. K., Wright, M. A., Chartrand, C. C., . . . , & Patterson, J. E. (2023). Characterization of organic crystals for second-harmonic generation. *Optics Letters*, *48*(22), 5855–5858. https://doi.org/10.1364/OL.506508

[12] Novikova, N. E., Sorokina, N. I., Verin, I. A., Alekseeva, O. A., Orlova, E. I., Voronkova, V. I., & Tseitlin, M. (2018). Structural reasons for the nonlinear optical properties of KTP family single crystals. *Crystals*, *8*(7), 283. https://doi.org/10.3390/cryst8070283

[13] Chen, M.-M., Zhou, S.-H., Wei, W., Wu, X.-T., Lin, H., & Zhu, Q.-L. (2021). AZn4Ga5Se12 (A=K, Rb, or Cs): Infrared nonlinear optical materials with simultaneous large second harmonic generation responses and high laser-induced damage thresholds. *Inorganic Chemistry*, *60*(13), 10038–10046. https://doi.org/10.1021/acs.inorgchem.1c01359

[14] Binks, D. J. (2021). Harmonic generation—Materials and methods. In C. Guo & S. C. Singh (Eds.), *Handbook of laser technology and applications* (pp. 233–253). CRC Press.

[15] Mamrashev, A., Nikolaev, N., Antsygin, V., Andreev, Y., Lanskii, G., & Meshalkin, A. (2018). Optical properties of KTP crystals and their potential for terahertz generation. *Crystals*, *8*(8), 310. https://doi.org/10.3390/cryst8080310

[16] Wang, J., Xiao, F., Yu, Z., Liang, K., & Chen, Y. (2026). Physics-informed finite element multi-scale modeling of light propagation using numerical approximation of slowly varying envelope. *Optics Express*, *34*(5), 9207–9220. https://doi.org/10.1364/OE.579547

[17] Ruziev, Z. J., Sapaev, B., Sapaev, I. B., Sapaev, U. K., Amanov, R., & Nazaraliev, D. (2022). On theory of approximation methods in the study of second harmonic generation of ultrashort laser pulses in periodic crystals. *AIP Conference Proceedings*, *2432*, 020008. https://doi.org/10.1063/5.0089970

[18] Li, W., Ma, Y., Feng, T., Du, Z., Liu, Y., Kalinin, S. V., . . . , & Li, Q. (2023). Delineating complex ferroelectric domain structures via second harmonic generation spectral imaging. *Journal of Materiomics*, *9*(2), 395–402. https://doi.org/10.1016/j.jmat.2022.09.011

[19] Xiao, F., Wang, J., Xiong, Z., & Chen, Y. (2025). Numerical approximation of slowly varying envelope in finite element electromagnetism: Ray-wave method of modeling multi-scale devices. *Optics Express*, *33*(6), 12603–12614. https://doi.org/10.1364/OE.550883

[20] Konforty, N., Cohen, M.-I., Segal, O., Plotnik, Y., Shalaev, V. M., & Segev, M. (2025). Second harmonic generation and nonlinear frequency conversion in photonic time-crystals. *Light: Science & Applications*, *14*(1), 152. https://doi.org/10.1038/s41377-025-01788-z

[21] Zimmerman, W. B. J. (2006). *Multiphysics modeling with finite element methods*. Singapore: Word Scientific. https://doi.org/10.1142/6141

[22] Andras, A., Popescu, F. D., Radu, S. M., Pasculescu, D., Brinas, I., Radu, M. A., & Peagu, D. (2024). Numerical simulation and modeling of mechano–electro–thermal behavior of electrical contact using COMSOL multiphysics. *Applied Sciences*, *14*(10), 4026. https://doi.org/10.3390/app14104026

[23] Gladyshev, S., Pashina, O., Proskurin, A., Nikolaeva, A., Sadrieva, Z., Petrov, M., . . . , & Frizyuk, K. (2024). Fast simulation of light scattering and harmonic generation in axially symmetric structures in COMSOL. *ACS Photonics*, *11*(2), 404–418. https://doi.org/10.1021/acsphotonics.3c01166

[24] Krupa, K., Fona, R., Tonello, A., Labruyère, A., Shalaby, B. M., Wabnitz, S., . . . , & Couderc, V. (2020). Spatial beam self-cleaning in second-harmonic generation. *Scientific Reports*, *10*(1), 7204. https://doi.org/10.1038/s41598-020-64080-7

[25] Dwi Astuti, W., Matsukuma, H., Nakao, M., Li, K., Shimizu, Y., & Gao, W. (2021). An optical frequency domain angle measurement method based on second harmonic generation. *Sensors*, *21*(2), 670. https://doi.org/10.3390/s21020670

[26] Strömberg, J. (2024). *Experimental optimization of second-order harmonic generation for higher-order generation applications*. Lund Reports on Atomic Physics (LRAP) https://lup.lub.lu.se/student-papers/search/publication/9177395

[27] Zu, R., Wang, B., He, J., Wang, J.-J., Weber, L., Chen, L.-Q., & Gopalan, V. (2022). Analytical and numerical modeling of optical second harmonic generation in anisotropic crystals using ♯SHAARP package. *npj Computational Materials*, *8*(1), 246. https://doi.org/10.1038/s41524-022-00930-4

How to Cite: Ahmed, N., Naeem, M., & Imran, T. (2026). Computational Investigation of Second Harmonic Generation in KTP Crystals Using COMSOL. *Journal of Optics and Photonics Research.* https://doi.org/10.47852/bonviewJOPR62028747